RSC Advances

PAPER

View Article Online
View Journal | View Issue

Cite this: *RSC Adv.*, 2026, **16**, 18232

Effects of activating agent and pyrolysis temperature on the pore structure and adsorption performance of sweet potato vine-based activated carbon

Wei Wei * and Na Ren

Received 6th February 2026
Accepted 30th March 2026

DOI: 10.1039/d6ra01057a

rsc.li/rsc-advances

China produces a large amount of sweet potato vines annually that require processing. In this study, sweet potato vine was used as a precursor to prepare activated carbons with two chemical activating agents ($ZnCl_2$ and K_2CO_3). The obtained activated carbons were characterized by N_2 adsorption/desorption isotherms, scanning electron microscopy (SEM), and Fourier transform infrared (FTIR) spectroscopy. The synthesized activated carbons were subsequently applied for the adsorption of methylene blue (MB). The effects of the activating agent and pyrolysis temperature on the properties and adsorption capacity of the activated carbons were investigated. The activated carbon prepared with K_2CO_3 at 800 °C (CK800) exhibits the highest surface area (1523.9 $m^2\ g^{-1}$) and total pore volume (0.7247 $cm^3\ g^{-1}$), and is composed of micropores and mesopores. In contrast, the sample activated with $ZnCl_2$ at 500 °C (CZn500) shows a surface area of 1347.2 $m^2\ g^{-1}$ and is dominated by mesopores with a mesopore volume of 1.0953 $cm^3\ g^{-1}$. Both activated carbons exhibited high adsorption capacities for methylene blue. Their adsorption isotherms followed the Langmuir model, with maximum adsorption capacities reaching 775.2 mg g^{-1} (CK800) and 400 mg g^{-1} (CZn500), respectively. The adsorption kinetics were consistent with the pseudo-second-order kinetic model. This is primarily attributed to their large BET surface area and high total pore volume. Simultaneously, mechanisms such as electrostatic attraction, π–π stacking, hydrophobic interaction, and hydrogen bonding also make important contributions to the materials' high adsorption performance. The prepared materials demonstrate that sweet potato vine can serve as a biomass feedstock for the production of activated carbon. Different preparation methods can impart distinct functionalities and physicochemical properties to the activated carbon. By selecting appropriate activating agents and pyrolysis temperatures, it is possible to successfully produce sweet potato vine-based activated carbon with high BET specific surface area, large pore volume, and excellent methylene blue adsorption performance.

1 Introduction

Dyes are extensively utilized across multiple industries including the textiles, leather, paper, and printing industries. However, their discharge poses significant environmental concerns, as dye contamination not only pollutes water bodies but also adversely affects aquatic flora and fauna, ultimately threatening human health through bioaccumulation in the food chain. The adsorption process serves as an effective method for treating dye-containing wastewater. Activated carbon has been widely employed as an adsorbent due to its excellent adsorption performance. However, its large-scale application remains limited by high production costs. Recently, researchers have shown growing interest in developing activated carbons from agricultural and industrial wastes, owing to their environmental sustainability, cost-effectiveness, and remarkable adsorption capacity. Various agricultural waste materials have been investigated as potential precursors, including sugarcane bagasse,[1,2] spent coffee grounds,[3] shells,[4–8] bamboo waste,[9] stones,[10–12] seeds,[13,14] peels,[15–18] stalk[19] and leaves.[20,21] Despite the substantial annual production of vine biomass, its utilization as a precursor for activated carbon preparation has received minimal attention. Only a limited number of studies have reported on this.[22]

China produces over 20 million tons of sweet potatoes annually, accounting for approximately 30% of the global yield. During harvesting, only a small portion of sweet potato vines (SPV) are utilized as animal feed, while the majority has traditionally been discarded through field burning – a practice now prohibited due to its environmental impact. SPV represent an

---

College of Biochemical Engineering, Beijing Union University, No. 18 Sanqu, Fatouxili, Chaoyang District, Beijing, 100023, China. E-mail: wlweiwei@buu.edu.cn; Fax: +86 10 52072157; Tel: +86 10 52072157

attractive raw material due to their low cost, abundant availability, renewability, and environmental friendliness. Chemically, SPV primarily consist of cellulose, hemicellulose, lignin, and minor mineral components.[23] These characteristics make SPV a promising precursor for activated carbon production. Nevertheless, limited studies have explored the utilization of SPV for this purpose. This study aimed to develop cost-effective activated carbon from SPV and evaluate its efficacy in removing textile dyes from aqueous solutions. The production of activated carbon from biomass typically involves two key steps: carbonization and activation. In this work, we employed a one-stage method using different chemical activating agents ($ZnCl_2$ and K_2CO_3), combining pyrolysis and activation in a single step to optimize energy efficiency. The results demonstrate that SPV can be effectively converted into high-quality activated carbon with large BET surface area and pore volume when processed with suitable activating agents and optimal pyrolysis temperatures. The resulting activated carbons exhibited excellent adsorption performance for methylene blue (MB) removal from aqueous solutions. These findings collectively demonstrate that SPV-derived activated carbon represents a promising and cost-effective adsorbent for practical applications.

2 Materials and methods

2.1 Material and reagents

SPV were collected from a local farm in Beijing, China. The fresh vines were first air-dried at ambient temperature, followed by oven-drying until constant weight was achieved. The dried material was then ground into fine powder. MB was procured from Shanghai Chemical Reagent Factory (Shanghai, China). All other chemical reagents, obtained from Lanyi Chemical Reagent Company (Beijing, China), were of analytical grade purity.

2.2 Preparation of activated carbons

The SPV powder was separately impregnated with $ZnCl_2$ and K_2CO_3 solutions for 24 hours, using mass ratios of 1 : 2 (SPV : $ZnCl_2$) and 1 : 1.5 (SPV : K_2CO_3), respectively. After impregnation, the samples were first air-dried at room temperature, followed by oven-drying at 100 °C for 12 hours. The dried mixtures then underwent simultaneous carbonization and activation under argon atmosphere at various predetermined temperatures. The resulting products were cooled, washed with deionized water, and finally oven-dried at 100 °C to constant weight. The obtained activated carbons were labeled as CZn*x* and CK*x*, where '*x*' represents the carbonization/activation temperature, and the prefixes indicate the activating agent used ($ZnCl_2$ or K_2CO_3, respectively).

2.3 Characterization of activated carbons

The surface morphology of activated carbons was examined using field-emission scanning electron microscopy (Sigma 300, Zeiss, Germany). Surface functional groups were characterized by Fourier-transform infrared spectroscopy (FT-IR, PerkinElmer, USA). Pore structure analysis was performed through nitrogen physisorption measurements using a Micromeritics ASAP 2020 analyzer (USA). Elemental analysis was performed using an elemental analyzer (EA 2400 II, PerkinElmer, USA) operating in CHN mode. Samples were combusted at 950 °C in an oxygen-rich atmosphere, and the resulting gases (CO_2, H_2O, and N_2) were separated by frontal chromatography and detected by a thermal conductivity detector (TCD). Acetanilide was used as a calibration standard.

For pH_{PZC} determination, selected activated carbons were added to 50 mL of 0.1 mol L^{-1} NaCl solution. The initial pH was adjusted to values ranging from 2 to 11 using 0.1 M HCl or NaOH solutions. The sealed flasks were then agitated in a thermostatic shaker for 48 hours. The pH_{PZC} was identified as the point where the final pH curve intersected the initial pH line ($\Delta pH = 0$).[24]

2.4 Adsorption experiments

For adsorption experiments, 50 mg of activated carbon samples were added to 250 mL glass flasks containing 100 mL of MB solutions at varying concentrations. The flasks were agitated in a thermostatic shaker until adsorption equilibrium was achieved. Sampling was performed at predetermined time intervals throughout the experiments. MB concentrations were quantified using a UV-vis spectrophotometer at 640 nm wavelength, with reference to a pre-established calibration curve. The equilibrium adsorption capacity, q_e (mg g^{-1}), was calculated using the following equation:

$$q_e = \frac{(C_o - C_e)V}{m} \tag{1}$$

The amount of adsorption at time t, q_t (mg g^{-1}) was calculated by the following equation:

$$q_t = \frac{(C_o - C_t)V}{m} \tag{2}$$

where C_o, C_e and C_t (mg L^{-1}) represent the MB concentration at initial, equilibrium and time t, respectively. V is the volume of the MB solution (L), and m is the mass of the carbon adsorbent (g).

The pH effect studies were conducted by mixing 50 mg of selected activated carbons with 100 mL MB solution. The solution pH was systematically adjusted to values between 2 and 10 using 0.1 M HCl or NaOH solutions.

CK800 and CZn500 were regenerated by soaking in a mixture of 0.1 M HCl and ethanol (50% v/v) with ultrasonic treatment for 30 minutes, followed by washing with deionized water until neutral. After drying, the regenerated samples were reused for the adsorption of MB to evaluate their reusability.

3 Results and discussion

3.1 Characterization of activated carbons

3.1.1 Characterization of elemental composition and structure in activated carbons. The elemental composition of activated carbons is summarized in Table 1. The carbon content of both samples exhibited an upward trend as the pyrolysis

Table 1 Elemental analysis results and porosity structures of activated carbons

	Elemental content (%)									
Samples	C	N	H	S_{BET} (m^2 g^{-1})	V_{total} (cm^3 g^{-1})	V_{micro} (cm^3 g^{-1})	V_{meso} (cm^3 g^{-1})	V_{mi} V_t^{-1} (%)	V_{me} V_t^{-1} (%)	Pore size (nm)
CK500	68.17	2.10	1.89	532.9	0.2846	0.2001	0.0845	70.31	29.69	2.14
CK600	72.67	1.92	1.67	684.6	0.3466	0.2722	0.0744	78.53	21.47	2.03
CK700	75.39	0.80	1.53	1193.1	0.5857	0.4368	0.1489	74.58	25.42	1.96
CK800	77.26	0.67	1.46	1523.9	0.7247	0.4266	0.2981	58.87	41.13	1.90
CZn400	58.92	2.28	2.26	671.0	0.3499	0.1279	0.2220	36.55	63.45	2.09
CZn500	60.70	2.10	1.54	1347.2	1.0953	0.000	1.0953	0	100	3.25
CZn600	62.61	2.31	1.62	1186.3	0.8367	0.0262	0.8105	3.13	96.87	2.82
CZn700	70.80	3.41	1.24	932.1	0.7658	0.0168	0.7490	2.19	97.81	3.28

temperature increased. In contrast, the nitrogen and hydrogen contents of the CK samples decreased with rising temperature, whereas those of the CZn samples showed no consistent pattern of change. These compositional changes are primarily attributed to the enhanced carbonization/activation and the elimination of volatile non-carbon components.

Fig. 1 presents the N_2 adsorption–desorption isotherms and corresponding pore size distributions of activated carbons prepared with different chemical activating agents and pyrolysis temperatures. As summarized in Table 1, these materials exhibit distinct BET surface areas, pore volumes, and average pore diameters. The results clearly demonstrate that the choice of chemical activator and thermal treatment conditions significantly influence the textural properties of the resulting activated carbons, producing materials with varying surface areas, pore size distributions, and pore volumes.

The N_2 adsorption–desorption isotherms of CK samples reveal a distinct evolution in pore structure with increasing carbonization temperature. CK500, CK600, and CK700 display typical Type-I isotherms, confirming their predominantly microporous nature, which is further supported by the pore size distribution and pore volume analyses. In contrast, the isotherms of CK800 exhibit hysteresis loops characteristic of Type-IV behavior, indicating the development of mesoporosity. CK800 features a mixed pore structure comprising both micropores and mesopores. This is likely attributable to the collapse of micropores or their blockage by volatiles under high temperatures. Both BET surface area and total pore volume demonstrate a positive correlation with pyrolysis temperature, increasing progressively from 500 to 800 °C. Remarkably, the sample CK800 achieved a maximum BET surface area of 1523.9 m^2 g^{-1} accompanied by a pore volume of 0.7247 cm^3 g^{-1}, significantly surpassing commercial activated carbons.[25,26] These findings underscore the critical role of pyrolysis temperature in determining pore characteristics. During thermal treatment, cellulose, hemicellulose, and lignin undergo degradation, dehydration, and carbonization, leading to carbon skeleton aromatization and pore development. The K_2CO_3 activator decomposes under argon atmosphere to form K, K_2O, CO, and CO_2. When the pyrolysis temperature exceeds the boiling point of potassium (759 °C), metallic potassium diffuses into the carbon matrix and reacts with the carbon, promoting the decomposition of volatile organic compounds and thereby forming a well-developed porous structure. Simultaneously, under high-temperature conditions, CO_2 can undergo an oxidation reaction with the disordered carbon present in the already formed biochar ($C + CO_2 \rightarrow 2CO$), which selectively etches the carbon skeleton, gradually forming and expanding its microporous and mesoporous structures.

The N_2 adsorption–desorption isotherms of CZn samples exhibit Type IV characteristics with distinct hysteresis loops in the relative pressure range of 0.55–0.99, confirming the presence of mesoporous structures. These observations are further supported by the corresponding pore size distribution and pore volume analyses. The textural properties show a temperature-dependent trend, where both BET surface area and total pore volume initially increase with carbonization temperature up to 500 °C before decreasing at higher temperatures. The maximum values achieved at 500 °C (1347.2 m^2 g^{-1}surface area and 1.0953 cm^3 g^{-1} pore volume) are comparable to mesoporous carbons (*e.g.*, 1267 m^2 g^{-1} and 0.96 cm^3 g^{-1}, respectively) as reported in literature.[27] The activation mechanism involves several key processes: (1) $ZnCl_2$, as a hygroscopic salt, induces cellular dehydration through osmotic pressure, enhancing precursor porosity; (2) during pyrolysis, water reacts with zinc chloride to form zinc oxide hydrate, simultaneously generating HCl that contributes to pore enlargement; (3) elevated temperatures (400–500 °C) intensify these reactions, promoting volatile compound formation and consequent pore development. The observed surface area reduction above 500 °C likely results from structural collapse of the porous framework under excessive thermal treatment.

Table 2 presents a comparative analysis of BET surface areas and total pore volumes for various biomass-derived activated carbons reported in previous studies. The results demonstrate that the SPV-based activated carbons prepared using $ZnCl_2$ and K_2CO_3 activation exhibit comparable textural properties to many other biomass-derived carbons, indicating their potential for adsorption applications.

3.1.2 Functional groups analysis.

The surface functional groups of the activated carbons were characterized by FT-IR spectroscopy, as presented in Fig. 2. Spectral analysis indicates that as the carbonization temperature increases, the intensity of organic functional groups in the CK samples shows a gradual

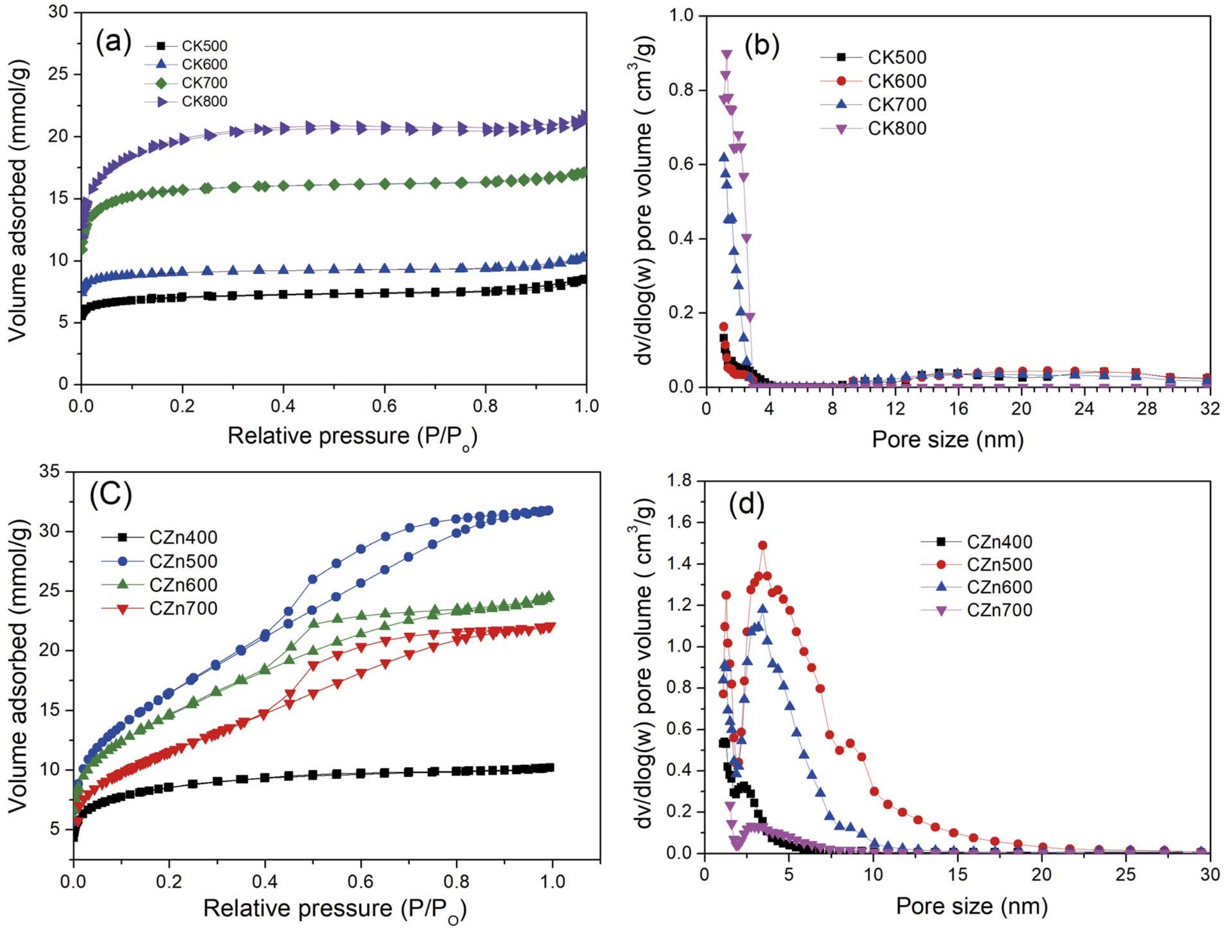

Fig. 1 N_2 adsorption–desorption isotherms and pore size distributions of activated carbons prepared with K_2CO_3 (a and b) and $ZnCl_2$ (c and d) at various carbonization/activation temperatures.

weakening trend, and when the temperature reaches 800 °C, the content of surface functional groups on the carbon material has significantly decreased (Fig. 2a). In contrast, the surface functionality of the CZn samples remained relatively stable across different temperatures (Fig. 2b). The FT-IR spectra exhibit characteristic absorption bands at: 3734 cm^{-1} (O–H stretching vibrations, hydroxyl groups); 1700 cm^{-1} (asymmetric stretching of $C{=}O$ bonds); 1537 cm^{-1} ($C{=}C$ aromatic ring vibrations); 1160 cm^{-1} (C–O stretching in ether/ester groups); 875 cm^{-1} (C–H bending vibrations). These spectral features confirm the presence of oxygen-containing functional groups and aromatic structures on the carbon surfaces. The temperature-dependent variations in peak intensities reflect the thermal stability differences between the two activation systems.

3.1.3 SEM and XRD analysis. The surface morphological structures of the raw SPV and the resulting carbons CK800 and CZn500 are shown in Fig. 3. The raw material possesses a hierarchical porous structure, whereas the activated carbon exhibits a well-developed micro- or mesopore structure. CK800 mainly shows micropores, while CZn500 is dominated by mesopores. Both types of activated carbon display smooth surfaces and uniform pores. The XRD spectra (Fig. S1) show that the activated carbons are amorphous, and the $ZnCl_2$-activated carbon contains a small amount of ZnO residue. In practice, sequential washing with hot $ZnCl_2$ solution, hot $ZnCl_2$–HCl solution, and hot water—as is common in the activated carbon industry—would be required to remove such residues prior to application.

3.2 Adsorptive removal of MB using activated carbons

3.2.1 Equilibrium data, isotherm and kinetics modelling. The adsorption capacities of different activated carbons for MB were measured, and the results are presented in Fig. S2 of the supporting materials. The findings indicate that the adsorption capacity for MB depends on the activation agent and pyrolysis temperature. Among the $ZnCl_2$ -activated carbons, CZn500 exhibited the highest adsorption capacity. The adsorbents followed a descending order of MB adsorption capacity: CZn500 > CZn600 > CZn700 > CZn400, which aligns with their BET surface area and total pore volume trends. Functional groups, pore structure, and BET surface area are the dominant factors influencing adsorption performance. FT-IR analysis confirmed that the four carbons possess similar functional groups. Therefore, the variations in MB adsorption capacities among them are primarily attributed to differences in BET surface area and total pore volume. The superior adsorption capacity of CZn500 can be ascribed to its highest BET surface area and pore

Table 2 Pore structure parameters and activation methods of activated carbons from various agricultural wastes

Material	Activation method	BET surface area (m^2 g^{-1})	Total pore volume (cm^3 g^{-1})	Average pore size (nm)	Reference
Rice husks	$ZnCl_2$	749.51	0.9956	1.53	2
Sugarcane bagasse	$ZnCl_2$	1386.58	0.9947	1.55	2
Loofah vine	KOH	904.6	0.677	2.99	28
Orange peel	H_3PO_4	79.73	0.03	20.1	29
Tamarind seeds	KOH	1172	0.618	2.1	13
Spent coffee grounds	KOH	827.91		2.7	3
Olive stone	H_3PO_4	710		1.25	11
Sugarcane bagasse	KOH	234.58			1
Bamboo biomass	Na_2SiO	381.6	0.52	5.43	9
Groundnut shell	KOH	412	0.322		7
Pine fruit shells	H_3PO_4	1022.13	0.566	2.215	6
Coconut shells	NaOH	345	0.2	1.92	8
Palm leave	KOH	540	0.261	5.13	21
Khat leaves	KOH	340	3.93	3.7	20
Black garlic peels		463.9	0.373		17
Banana peels	H_3PO_4	867	0.032		16
Palm stones	CO_2	19.53	0.007	1.43	12
Coconut shells	Alkali from cocoa pod husks	1250.20	0.61	2.754	30
Plane tree seeds	NaOH	1508.6	0.7063	2.0462	26
Cellulose	H_3PO_4	561			31
Commercial activated carbon		1185	0.57		26
Sweet potato vine	$ZnCl_2$	1347.2	1.0953	3.25	This work
Sweet potato vine	K_2CO_3	1523.9	0.7247	1.90	This work

volume, which provide more active sites for adsorption. Similarly, among the K_2CO_3-activated carbons, sample CK800 exhibited the highest MB adsorption capacity, corresponding to its largest BET surface area and total pore volume. However, samples with similar specific surface areas (*e.g.*, CK700 and CZn600) did not exhibit identical adsorption capacities, indicating that the adsorption process is influenced by factors beyond surface area. This discrepancy might be related to differences in their pore size distributions, particularly in the micropore region. As shown in Table 1, CK700 possesses a substantial micropore volume of 0.4368 cm^3 g^{-1}, accounting for 74.58% of its total pore volume, whereas CZn600 has a much lower micropore volume of only 0.0262 cm^3 g^{-1}, with mesopores dominating its pore structure (0.8105 cm^3 g^{-1}, 96.9% of total pore volume).

According to Polanyi's adsorption potential theory,[32] the adsorption potential ε is inversely related to pore size (d_p, nm). In microporous carbons, the characteristic adsorption energy E_0 (kJ mol^{-1}) follows the Dubinin–Stoeckli relationship:[33,34]

$$E_0 = 15.8/d_p \tag{3}$$

This relationship indicates that micropores (<2 nm) generate significantly higher adsorption potentials than mesopores (2–50 nm). For dye molecules such as MB (molecular dimensions ~1.4 nm × 0.6 nm × 0.4 nm), the enhanced interaction arises

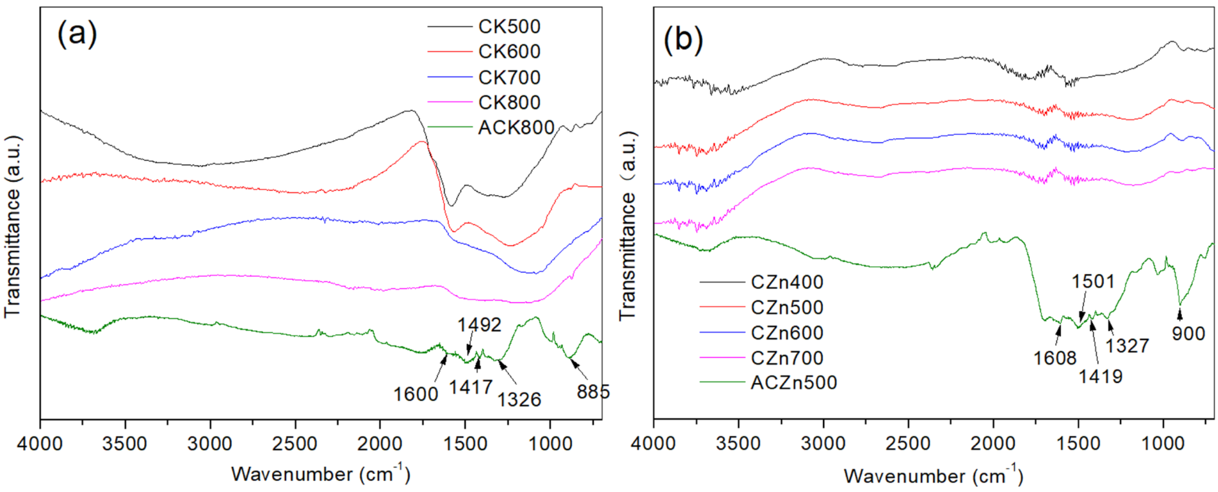

Fig. 2 FT-IR spectra of the activated carbons, ACK800 (a) and ACZn500 (b) are the activated carbon after MB adsorption.

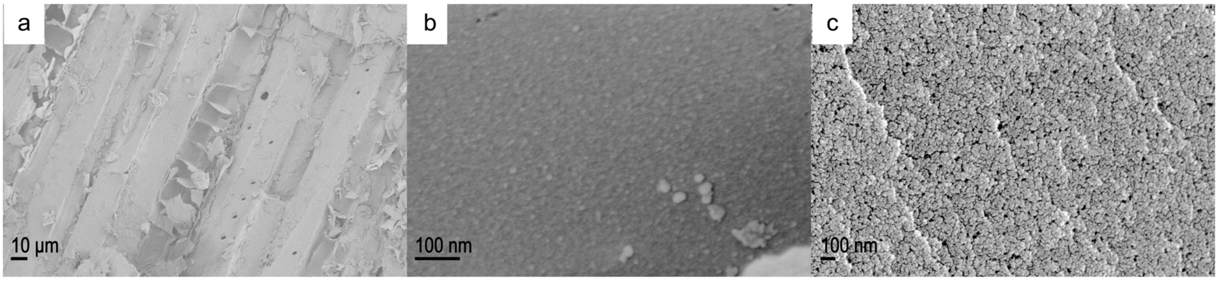

Fig. 3 SEM images SPV and activated carbons: (a) SPV, (b) CK800, (c) CZn500.

from the superposition of Lennard-Jones potentials from opposing pore walls,[35] leading to strong adsorption through micropore filling at low concentrations.[36]

Thus, the superior adsorption capacity of CK700 (478 mg g^{-1}) compared to CZn600 (369 mg g^{-1}) is related to its abundant micropore structure, which provides a higher adsorption potential and facilitates effective micropore filling. In contrast, the mesopore-dominated structure of CZn600 limits its adsorption primarily to surface coverage, resulting in a lower overall capacity despite its comparable specific surface area.

FTIR analysis was conducted to further elucidate the adsorption mechanism. After MB adsorption (Fig. 2), several new peaks characteristic of MB appeared at approximately 1500, 1417, 1395, 1330, and 880–800 cm^{-1}, corresponding to aromatic C=C stretching, and C–N stretching/–CH$_3$ bending.[37,38] Notably, the peak at 1417 cm^{-1} shifted from its typical position (*ca.* 1395 cm^{-1}), indicating electrostatic interactions between the cationic MB molecules and the carbon surface.[39,40] Meanwhile, the aromatic C=C peak at ~1600 cm^{-1} exhibited enhanced intensity and a slight shift, suggesting π–π stacking interactions between MB and the graphitic microcrystallites of the activated carbon.[41,42] Raman spectra (Fig. S3) show that the activated carbon is composed mainly of amorphous carbon with some graphitic crystallites. The effect of solution pH on adsorption capacity (Fig. 6b) confirms that electrostatic attraction plays a significant role, particularly for CZn500, where the surface charge transitions from positive to negative around its pH$_{\text{PZC}}$ of 6.68. Furthermore, the hydrophobic nature of the carbon surface promotes hydrophobic interactions with the MB molecule. These results suggest that MB adsorption is governed by a combination of π–π stacking and electrostatic interactions, complementing the physical adsorption associated with the

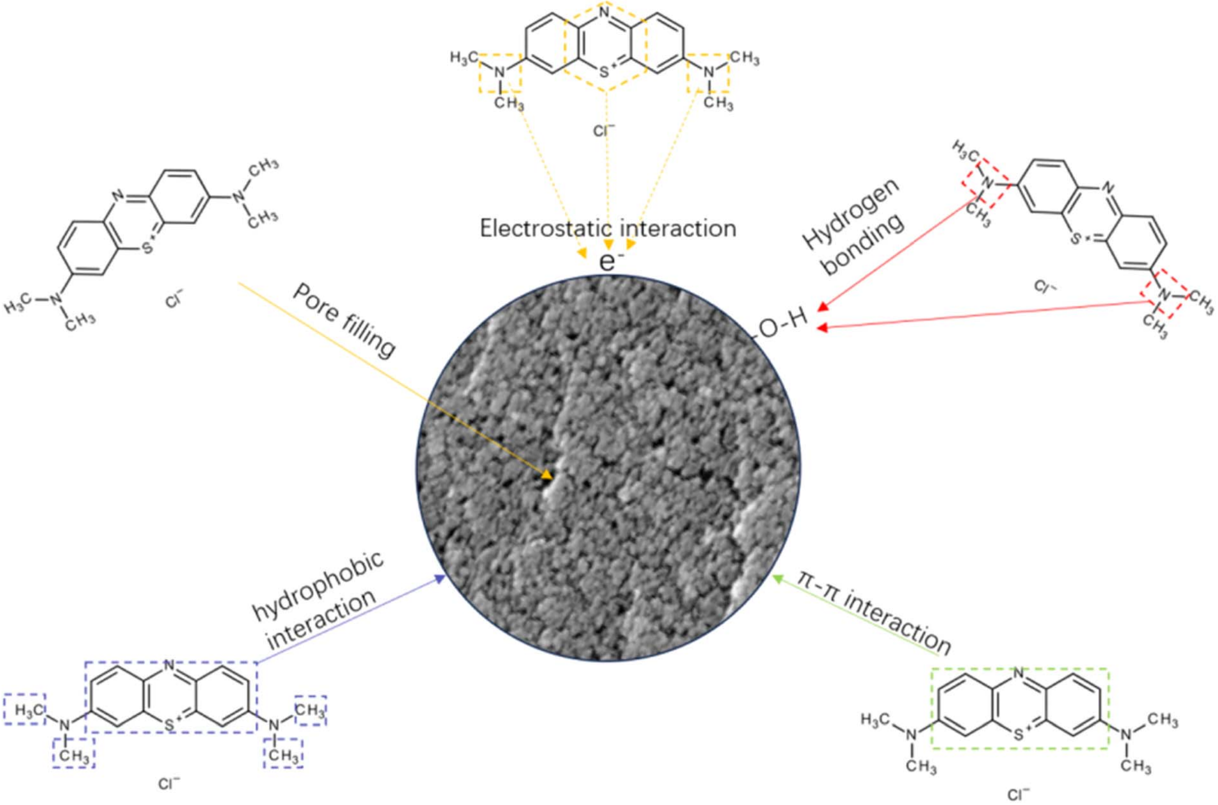

Fig. 4 Proposed adsorption mechanism of activated carbon for methylene blue.

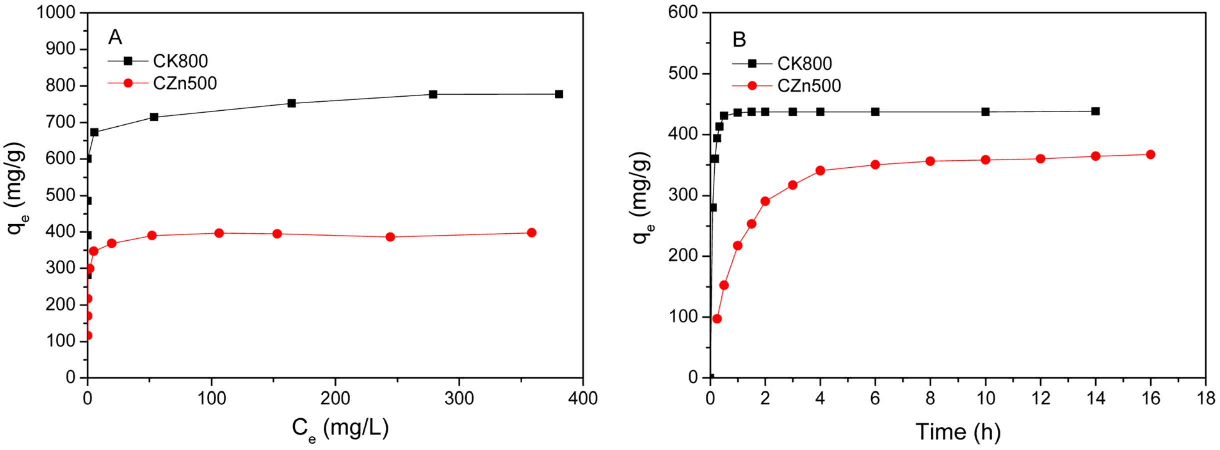

Fig. 5 Effects of MB concentration (A) and contact time (B) on the adsorption of onto activated carbons.

pore structure. Based on the characterization results and adsorption experiments, a multi-faceted adsorption mechanism is proposed, as illustrated in Fig. 4. The MB adsorption capacity of the prepared activated carbon indicates promising performance under the specific batch conditions used in this study.[31,43–48]

The activated carbons CK800 and CZn500 were selected for adsorption studies. The adsorption capacity of CK800 and CZn500 were maintained about 75% (535.8 mg g^{-1}) and 78% (304.2 mg g^{-1}) respectively after four adsorption-regeneration cycles, showing good reusability. Fig. 5 presents the MB adsorption isotherms and kinetics for these two materials. The isotherm data were analyzed using the Langmuir, Freundlich and Temkin adsorption models to characterize the equilibrium distribution of adsorbed molecules between the liquid and solid phases. The calculated isotherm parameters and corresponding correlation coefficients (R^2) for tested models are presented in Table 3. As summarized in Table 3, the Langmuir isotherm model provided the best fit to the experimental data, demonstrating excellent linearity ($R^2 = 0.999$) across the entire concentration range studied. This strong correlation suggests that MB adsorption on both CK800 and CZn500 is reasonably well described by the Langmuir equation over the tested concentration range, although biochar and activated carbon often possess heterogeneous surfaces.

According to the Langmuir model calculations, the maximum adsorption capacities of CK800 and CZn500 are 775.2 mg g^{-1} and 400.0 mg g^{-1}, respectively. To investigate the adsorption mechanism, two kinetic models – pseudo-first-order and pseudo-second-order – were employed to analyze the adsorption process. The results demonstrate that MB adsorption followed the pseudo-second-order kinetic model, with the corresponding parameters summarized in Table 4.

To further elucidate the rate-controlling steps, the kinetic data were fitted to the intraparticle diffusion model (Fig. S4 and Table 5) and Boyd model (Fig. S5). The adsorption process of CK-800 toward the target adsorbate exhibits a distinct three-stage characteristic, governed by a combined rate control of film diffusion and intraparticle diffusion. The fitting results of the intraparticle diffusion model show that in the first stage, the rate constant $k_{\mathrm{id1}} = 544.29$ mg g^{-1} $h^{-0.5}$ and the intercept $C_1 = 126.62 > 0$, indicating that film diffusion (boundary layer effect) dominates the initial stage with a fast adsorption rate. In the second stage, the rate constant decreases to $k_{\mathrm{id2}} = 174.90$ mg g^{-1} $h^{-0.5}$ and the intercept $C_2 = 308.59 > 0$, suggesting that intraparticle diffusion becomes the main rate-controlling step, while film diffusion still contributes. In the third stage, the rate constant approaches zero ($k_{\mathrm{id3}} = 1.29$), indicating that adsorption reaches equilibrium. The progressive decrease in rate constants ($k_{\mathrm{id1}} > k_{\mathrm{id2}} \gg k_{\mathrm{id3}}$) and the gradual increase in intercepts ($C_1 < C_2 < C_3$) across the three stages are consistent with the typical characteristics of multi-step adsorption. Meanwhile, the Boyd plot is nonlinear and does not pass through the origin, further confirming that intraparticle diffusion is not the sole rate-controlling step, and that the microporous structure of CK-800 hinders pore diffusion, causing deviation from the ideal Fickian diffusion behavior. Integrating the results from both models, the adsorption process of CK-800 is governed by a combined control of film diffusion and intraparticle diffusion, with hindered diffusion within the microporous structure being the fundamental reason for the reduced intraparticle diffusion rate.

Table 3 Isotherm model parameters for the adsorption of MB onto CK800 and CZn500

	Langmuir			Freundlich			Temkin		
Samples	$q_{\max}$ (mg g^{-1})	K_L (L g^{-1})	R^2	K_F ((mg g^{-1}) (L $mg^{-1})^{1/n}$)	n	R^2	K_T (L g^{-1})	B (J mol L^{-1})	R^2
CK800	775.2	0.364	0.999	734.689	29.507	0.987	5.19×10^{11}	23.610	0.983
CZn500	400.0	1.923	0.999	242.759	8.326	0.600	1.06×10^{4}	28.132	0.754

Table 4 Kinetic model parameters for the adsorption of MB onto CK800 and CZn500

	Pseudo-first-order model			Pseudo-second-order model		
Samples	q_e (mg g^{-1})	k_1 (h^{-1})	R^2	q_e (mg g^{-1})	k_2 (g mg^{-1} h^{-1})	R^2
CK800	7.258	0.635	0.339	438.6	0.1165	0.999
CZn500	176	0.324	0.939	383.1	0.385	0.999

Table 5 Fitting parameters of the Webber–Morris intra-particle diffusion model

	First stage of intra-particle diffusion			Second stage of intra-particle diffusion			Third stage of intra-particle diffusion		
Samples	K_{id1} (mg g^{-1} h$^{-0.5}$)	C_1	R^2	K_{id2} (mg g^{-1} h$^{-0.5}$)	C_2	R^2	K_{id3} (mg g^{-1} h$^{-0.5}$)	C_3	R^2
CK800	544.29	126.62	0.964	174.90	308.59	0.932	1.29	433.82	0.284
CZn500	207.93	0.5422	0.9903	85.84	168.85	0.9997	12.12	319.06	0.9531

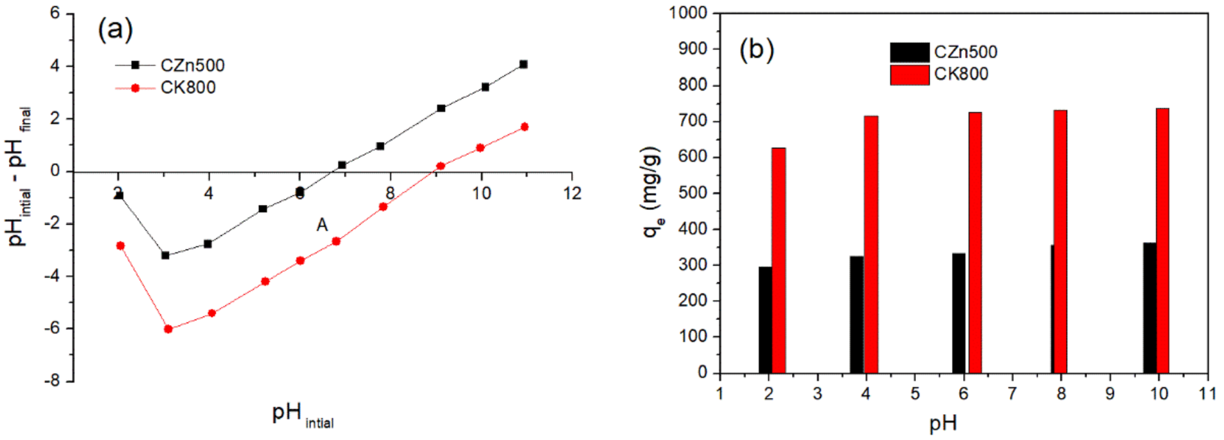

Fig. 6 The pH_{PZC} of activated carbons (a) and effect of solution pH on MB adsorption onto activated carbons (b).

For the mesoporous CZn-500, the adsorption process toward the target adsorbate is dominated by intraparticle diffusion. The fitting results of the intraparticle diffusion model show three distinct linear stages. In the first stage, the intercept $C_1 = 0.5422$ is very close to zero, indicating that film diffusion (boundary layer effect) makes a negligible contribution in the initial stage. In the second stage, the rate constant decreases to $k_{id2} = 85.84$ mg g^{-1} h$^{-0.5}$, and intraparticle diffusion becomes the main rate-controlling step. In the third stage, the rate constant $k_{id3} = 12.12$ mg g^{-1} h$^{-0.5}$ remains relatively high compared to microporous materials, reflecting the favorable diffusion properties enabled by the mesoporous structure. The Boyd plot exhibits good linearity ($R^2 = 0.931$) with an intercept of 0.278, further confirming that intraparticle diffusion is the predominant rate-controlling step, with only a minor contribution from boundary layer effects.

In comparison with the microporous material CK-800, which exhibits a combined control mechanism of film diffusion and intraparticle diffusion, the mesoporous structure of CZ500 effectively reduces pore diffusion resistance, leading to adsorption behavior that more closely approximates the ideal intraparticle diffusion-controlled model.

3.2.2 Effect of pH.

The solution pH can influence the adsorption performance by altering the surface charge characteristics of the adsorbent. Fig. 6b presents the pH-dependent adsorption behavior of MB on CZn500 and CK800 across the pH range of 2–10. As the pH value increases, the adsorption capacity shows a slight increase, with this growth trend being more pronounced under lower pH conditions. The point of zero charge (pH_{PZC}) determinations (Fig. 6a) revealed values of 6.68 for CZn500 and 8.9 for CK800. When solution pH exceeded these pH_{PZC} values, the adsorbent surfaces acquired a net negative charge, facilitating enhanced electrostatic attraction with the cationic MB molecules. Conversely, at pH conditions below the pH_{PZC}, the positively charged adsorbent surfaces exhibited reduced affinity for MB due to electrostatic repulsion. These findings demonstrate that electrostatic interactions play a role in the MB adsorption mechanism.

4 Conclusion

Activated carbons were prepared from SPV using $ZnCl_2$ and KCO_3 as activating agents, respectively. Their performance as adsorbents was then evaluated for the removal of MB from aqueous solutions. Experimental results demonstrate that the prepared activated carbons possess high surface areas and total pore volumes. The activated carbon synthesized with K_2CO_3 predominantly features micropores at lower temperatures, while exhibiting a micro-mesoporous composite structure at elevated temperatures. As the pyrolysis temperature increases, the specific surface area and total pore volume of activated carbons both show an increasing trend. The sample prepared at 800 °C achieved a surface area of 1523.9 $m^2\ g^{-1}$ with a total pore volume of 0.7247 $cm^3\ g^{-1}$. In contrast, the $ZnCl_2$-activated carbon exhibits a mesopore-dominated porous structure, with the sample treated at 500 °C showing the highest specific surface area and mesopore volume, reaching 1347.2 $m^2\ g^{-1}$ and 1.0953 $cm^3\ g^{-1}$, respectively. Both the activated carbons exhibited exceptional adsorption performance for methylene blue. The adsorption process was influenced by initial dye concentration, contact time, and solution pH. The adsorption process was well described by the Langmuir isothermal model, suggesting a homogeneous monolayer adsorption. Kinetic studies indicated that the adsorption followed pseudo-second-order kinetics.

This approach effectively addresses the challenges related to the disposal and management of agricultural waste. Furthermore, it contributes to lower production costs, diversifies the raw material sources for activated carbon, and may offer potential for supporting the treatment of dye-contaminated wastewater.

Author contributions

Wei Wei: supervision, funding acquisition, conceptualization, writing – original draft. Na Ren: data curation, formal analysis, writing – review & editing.

Conflicts of interest

The authors declare no competing financial interest.

Data availability

The data that support the findings of this study are available from the corresponding author upon reasonable request.

Supplementary information (SI): XRD, Raman, adsorption isotherms, fitting curves of Webber–Morris intra-particle diffusion and Boyd model. See DOI: https://doi.org/10.1039/d6ra01057a.

Acknowledgements

This work was financially supported by the National Natural Science Foundation of China (No. 51772031).

References

1 D. Dermawan, S. I. C. Karno, T. A. Ramadani, D. R. Widiana, A. C. Ni'am, Y.-F. Wang and A. Setiawan, *Miner. Eng.*, 2025, **232**, 109575.

2 E. R. Raut, M. A. Bedmohata and A. R. Chaudhari, *Mater. Today: Proc.*, 2022, **66**, 1875–1884.

3 R. Campbell, B. Xiao and C. Mangwandi, *J. Environ. Manage.*, 2024, **366**, 121682.

4 I. A. Olowonyo, K. K. Salam, M. O. Aremu and A. Lateef, *Waste Manag. Bull.*, 2024, **1**, 217–233.

5 R. S. Brishti, R. Kundu, M. A. Habib and M. H. Ara, *Results Chem.*, 2023, **5**, 100727.

6 I. Hamadneh, R. A. Abu-Zurayk, A. Aqel, A. Al-Mobydeen, L. Hamadneh, Y. Al-Dalahmeh, F. Hannoon, R. Albuqain, S. Alsotari and A. H. Al-Dujaili, *Desalination Water Treat.*, 2022, **264**, 293–306.

7 D. Mani, D. Elango, A. Priyadharsan, L. A. Al-Humaid, N. D. Al- Dahmash, S. Ragupathy, P. Jayanthi and Y.-H. Ahn, *Environ. Res.*, 2023, **231**, 116026.

8 J. Saleem, Z. K. B. Moghal, S. Pradhan and G. McKay, *RSC Adv.*, 2024, **14**, 33797–33808.

9 Y. Guo and Q. Wang, *Environ. Technol. Innovation*, 2023, **32**, 103318.

10 J. De Smedt, P. J. Arauzo and F. Ronsse, *Bioresour. Technol.*, 2025, **419**, 132040.

11 K. Haddad, M. Ghafer, H. Salman and H. El-Rakkad, *Results Chem.*, 2025, **14**, 102137.

12 A. A. Ali and H. M. Abdul-Hameed, *Desalination Water Treat.*, 2025, **321**, 100951.

13 P. Janthabut, P. Athikaphan, P. Jekruk, P. Kanchunsi, P. Kongkoed, S. Nijpanich, S. Theerakulpisut, A. Neramittagapong and S. Neramittagapong, *Environ. Chall.*, 2025, **20**, 101243.

14 P. M. Thabede and N. D. Shooto, *S. Afr. J. Chem. Eng.*, 2025, **53**, 256–266.

15 A. Martín-Lorenzo, M. Hoyos and A. Álvarez-Gómez, *J. Anal. Appl. Pyrolysis*, 2025, **192**, 107280.

16 S. Phal, C. Guigui, A. Didi, R. Tan and Y. Bessiere, *J. Water Proc. Eng.*, 2025, **77**, 108495.

17 D. Duan, S. Xu, Y. Zhou, H. Mo, W. Yang, Y. Zhang and R. Ruan, *J. Anal. Appl. Pyrolysis*, 2025, **191**, 107229.

18 A. S. Almaghrabi, E. M. Bakhsh, K. Akhtar, M. A. Alghamdi and S. B. Khan, *Results Chem.*, 2025, **15**, 102277.

19 B. Ren, X. Han, Y. Jin, Y. Zhang, X. Song, L. Zhao and R. Liu, *J. Environ. Chem. Eng.*, 2025, **13**, 118989.

20 A. A. Alswat, A. M. Ashmali, T. M. Alqasmi, H. R. Alhassani and F. T. Alshorifi, *Heliyon*, 2023, **9**, e14301.

21 M. A. Islam, M. K. Nazal, A. A. Akinpelu, M. Sajid, N. A. Alhussain, R. E. K. Billah and L. Bahsis, *Diamond Relat. Mater.*, 2024, **147**, 111375.

22 G. Qin, C. Wang, Q. Yang and W. Wei, *Desalination Water Treat.*, 2023, **283**, 237–246.

23 T. Wang, X. Dong, Z. Jin, W. Su, X. Ye, C. Dong and Q. Lu, *Bioresour. Technol.*, 2015, **192**, 799–801.

24 F. Marrakchi, M. Bouaziz and B. H. Hameed, *Colloids Surf., A*, 2017, **535**, 157–165.

25 K. Kuśmierek, L. Dąbek and A. Świątkowski, *Desalination Water Treat.*, 2025, **321**, 100996.

26 V. Dodevski, M. Marinović-Cincović and B. Janković, *Carbon Resour. Convers.*, 2025, 100377.

27 M. Marzuki, A. H. Jawad, N. I. I. M. Zazulir, R. R. R. Deris, R. Wu and Z. A. Alothman, *Diamond Relat. Mater.*, 2025, **159**, 112869.

28 C. Wang, Q. Yang, N. Ren, Z. Zhao, W. Wei and G. Qin, *Chem. Eng. Commun.*, 2022, **209**, 62–68.

29 A. I. Licona-Aguilar, A. M. Torres-Huerta, M. A. Domínguez-Crespo, M. L. X. Negrete-Rodríguez, E. Conde-Barajas, S. B. Brachetti-Sibaja and A. E. Rodríguez-Salazar, *Chem. Eng. J.*, 2024, **492**, 152102.

30 D. T. Ojo, O. S. Amuda, K. K. Salam, O. F. Oyediran and B. B. Yekini, *Next Nanotechnol.*, 2025, **8**, 100198.

31 N. Anter, A. Hannioui, A. Medaghri-Alaoui and M. Ghazoui, *RSC Adv.*, 2025, **15**, 49780–49795.

32 M. Polanyi, *Science*, 1963, **141**, 1010–1013.

33 M. M. Dubinin, *Carbon*, 1989, **27**, 457–467.

34 D. E. Morel and F. Stoeckli, *Chimia*, 1980, **34**, 503–504.

35 R. D. Kaminsky, W. C. Conner and E. Maglara, *Langmuir*, 1994, **10**, 1556–1565.

36 C. H. Giles, T. H. MacEwan, S. N. Nakhwa and D. Smith, *J. Chem. Soc.*, 1960, 3973–3993, DOI: 10.1039/JR9600003973.

37 A. Kumar and K. P. Srivastava, *Orient. J. Chem.*, 2002, **18**, 2.

38 A. Javed, M. Islam, Y. O. Al-Ghamdi, M. Iqbal, M. Aljohani, S. Sohni, S. S. A. Shah and S. A. Khan, *Int. J. Biol. Macromol.*, 2024, **256**, 128363.

39 Y. Li, Q. Du, T. Liu, J. Sun, Y. Wang, S. Wu, Z. Wang, Y. Xia and L. Xia, *Carbohydr. Polym.*, 2013, **95**, 501–507.

40 A. Bhattacharyya, S. Ghorai, D. Rana, I. Roy, G. Sarkar, N. R. Saha, J. T. Orasugh, S. De, S. Sadhukhan and D. Chattopadhyay, *Mater. Chem. Phys.*, 2021, **260**, 124090.

41 C. E. Anson, C. S. Creaser and G. Richard Stephenson, *Spectrochim. Acta, Part A*, 1996, **52**, 1183–1191.

42 W. Xiao, X. Jiang, X. Liu, W. Zhou, Z. N. Garba, I. Lawan, L. Wang and Z. Yuan, *J. Clean. Prod.*, 2021, **284**, 124773.

43 D. D. Anuse, S. A. Patil, A. A. Chorumale, A. G. Kolekar, P. P. Bote, L. S. Walekar, M. G. Mali and S. P. Pawar, *Clean. Water*, 2025, **4**, 100118.

44 S. R. Mishra, T. Mandal, P. Kumar, V. Verma, R. N. Senapati, M. Kumar and V. Singh, *Surf. Interfaces*, 2025, **69**, 106770.

45 Y. Liu, J. Wang, L. Xu, D. Qian and Y. Mu, *J. Environ. Chem. Eng.*, 2025, **13**, 118317.

46 A. A. R. Andrade, M. C. Silva, L. H. S. Crespo, T. L. Silva, A. L. Cazetta, L. Spessato and V. C. Almeida, *J. Mol. Liq.*, 2025, **427**, 127435.

47 X. Fan, B. Qiu, X. Tian and X. Yang, *Microporous Mesoporous Mater.*, 2025, **394**, 113625.

48 M. Usama, S. Atta, M. N. Qasim, A. Q. Alshammari, A. K. Alanazi, N. A. Khan, M. Mateen and M. N. Akhtar, *RSC Adv.*, 2025, **15**, 46553–46569.